Chapter 5
Nonlinear Problems in Piezoelectric Harvesters Under Magnetic Field

Erol Kurt and Yunus Uzun

Abstract This chapter focuses on the nonlinear problems in the piezoelectric harvester systems under the magnetic field. In this manner, the chapter initially mentions an introductory section on the studies of piezoelectric harvester dynamics. After the introductory section, the basic properties of the piezoelectric systems and their energy harvester applications will be presented. Since the harvesters have a complicated structure under the magnetic field, the electromagnetic design, modeling and algebraic studies of a novel harvester study will be pointed out. After the presentation of a theoretical outline on the harvester systems, the experimental setups will be explained in detail. Thus, a complete picture of the problem will be produced in order to sustain a comparable study on the theory and experiment. The main dynamic quantities such as displacement and velocity of the vibrating piezoelectric layer as function of the system parameters will be explored. According to results, the effect of periodic magnetic flux can give varieties of responses from regular dynamics to chaotic one. Phase space constructions, Poincare sections and FFTs are evaluated depending on the parameter sets including the excitation frequency f, amplitude Uc of electromagnet and the distance d. It is proven that the periodic magnetic flux can exert high frequency velocity fluctuations nearby the minimal and maximal values of the velocity, whereas the situation differs for the position. Therefore it will be pointed out that the magnetic field mostly governs the velocity by yielding complicated vibrations. According to the detailed analyses, the FFTs prove the high frequency responses in addition to the main frequency. When f differs from the natural frequency of the system f_0, the responses become chaotic. It is proven that lower and higher frequency fluctuations in displacement and velocity, which are different from f_0 decrease the electrical power harvested by the

---

E. Kurt (✉)
Technology Faculty, Department of Electrical and Electronics Engineering,
Gazi University, 06500 Teknikokullar, Ankara, Turkey
e-mail: ekurt52tr@yahoo.com

Y. Uzun
Faculty of Engineering, Department of Electrical and Electronics Engineering,
Aksaray University, Aksaray, Turkey
e-mail: yunusuzun@aksaray.edu.tr

N. Bizon et al. (eds.), *Energy Harvesting and Energy Efficiency*,
Lecture Notes in Energy 37, DOI 10.1007/978-3-319-49875-1_5

piezoelectric pendulum. Indeed, it is remarkable to get a relation between the rms values of displacement/velocity and the harvested power according to the measurements. Thus this relation can be used to estimate the power output in harvester systems. The piezoelectric harvester generates much energy when f is closed to f_0 and the distance to the magnetic device should be closer in order to decrease the nonlinearities in displacement and velocity. The pendulum-like harvesters as the most preferable ones can be applied to many devices or units as a power source. The maximal power for these magnetically-excited structures can be estimated by the system parameters. At the end of the chapter, the recent techniques of maximal power point tracking (MPPT) and proposed controller units are explained for the piezoelectric harvester systems in order to optimize the harvested power.

Keywords Piezoelectric harvester · Magnetic field · Nonlinearity · Attractor · Maximal power point tracking

Abbreviations and Acronyms

MEMS	Micro-electro-mechanical system
CDRG	Coulomb-damped resonant generator
DAQ	Data acquisition
FEM	Finite element method
FFT	Fast Fourier transform
MPPT	Maximal power point tracking
RMS	Root mean square
SIDO	Single inductor dual output
SSPB	Single-supply pre-biasing
THD	Total harmonic distortion
VDRG	Velocity-damped resonant generator

5.1 Introduction

In parallel with the improvements on the fields of smart material and energy material technologies, there exists a growing interest on the harvester systems, world-widely [1–3]. The energy harvesting studies mainly focus on three types of harvester systems: Piezoelectric, electromagnetic, and electrostatic [4–7]. Although the piezoelectric materials have a complicated material production procedure (which makes the piezo-structures much expensive than the others in any induction system), higher energy densities from the piezo-systems can be available [8–10]. Table 5.1 gives brief information on the energy densities of three harvesting types.

Piezoelectric systems are more convenient than electromagnetic ones for MEMS applications, because of the problems in magnets miniaturization with current state-of-the-art microfabrication processes [12]. Piezoelectric materials can

Table 5.1 Maximum energy density of three types of energy harvesting [11]

Type	Power equation	Practical maximum (mJ/cm^3)	Theoretical maximum (mJ/cm^3)
Electromagnetic	$E = B^2/2\mu_0$	4	400
Electrostatic	$E = 1/2\varepsilon\, E^2$	4	44
Piezoelectric	$E = \sigma_y^2\, k^2/2Y$	17.7	335

efficiently convert vibrations to electrical energy with relatively high output voltage but without any other voltage source [5]. In addition to above-mentioned superiorities of piezoelectrics, the advances in solid material behavior shed a light to combine the dynamical aspects of solids and the piezoelectric features in order to explain the energy harvesting mechanism behind the solid/piezo structures. At this point, there is very thin separation between a piezoelectric dynamical system and a piezoelectric harvester system: Mainly if a piezoelectric system can harvest energy from any ambient effect such as wind, human movement, seismic forces, water flow, and traffic, etc. [13–16], it is classified as a piezoelectric harvester, otherwise any other systems related to the piezo-structures can be acceptable as piezoelectric dynamic system. From this point, any piezoelectric harvester system is also a piezoelectric dynamic system, thereby the dynamical tools to explain the physics and engineering of energy production and fluctuation phenomena can be used to determine the amplitude/power or velocity/power relations [17, 18].

According to the dynamics of a fluctuating beam, there exists a wide literature, which has been mostly studied by physicists and mechanical engineers [19–21]. According to their approach, a spring-mass model can be used to understand the dynamics of a fluctuating beam under an external stress and damping effect. Equivalently, a basic pendulum model has also been used to identify the dynamical features of the fluctuating beam in some other researches [22–24]. According to these two models, the basic harmonic motion is described by the restoring force of spring or gravitation.

The piezoelectric beams have certain force-voltage relation. Indeed, when the beam is buckled by an external stress (i.e. mechanical, magnetic, electrical, magnetic, etc.), the beam terminals induce a voltage. Note that if the buckled beam then becomes static in any position, it does not induce any potential difference since there is no certain electrical dipole moment inside the crystal structure of piezo-material. Note also that the polarization direction also plays an important role to have an efficient voltage production. Strictly speaking the force should be in the polarization direction of the electrical dipoles. In the case of magnetic stress, the magnetic flux should be oriented in such a way that the permanent magnet(s) should buckle the piezoelectric beam in the polarization direction. Therefore the poles of the magnet(s) and the external magnetic flux direction should be well-simulated [25].

In the following section, initially some basic information on the electromagnetic design, modeling and simulation will be given. Next section will handle the experimental techniques on the piezoelectric systems. Section 5.4 explains the methods of nonlinear analyses, which are used in the fluctuation studies of piezoelectric systems. Section 5.5 introduces some piezoelectric systems and explains their nonlinear analyzes. While the nonlinear analyzes are discussed in the next section, Sect. 5.7 explains the dependence of dynamics and power to the system parameters. Section 5.8 presents MPPT techniques for piezoelectric harvester systems. Finally the conclusions give the main results of the chapter and some clues on the future perspectives.

5.2 Electromagnetic Design, Modeling and Simulation

The electromagnetic (EM) design is very important for a piezoelectric system in order to estimate the experimental results and the optimization of the system. If the EM design is made in a proper way, it helps to decrease the time consumption in the construction of the setup and the experimental researches. According to the literature there exists some tools to make electromagnetic design and simulation. However, all of them use the finite element method (FEM) because of its reliability and solution speed. Before starting any solution, the geometry and material assignment should be made correctly. Since the magnetic force depends on the distance between the magnetic sources and ferromagnetic bodies strictly, especially the magnetic bodies in the model should be positioned in the correct position in order to estimate the correct magnetic force f_m. In Fig. 5.1, a representative mesh structure is shown. Note that the number of mesh elements can be useful for the FEM simulation. Extremely large elements yield to long runs of computer and the results cannot be obtained in the proper time duration, whereas an optimized number of elements yield to both correct and faster solution.

In order to determine the number of mesh elements, one can assign different numbers to FEM programme and look for the simulation results. If there is a valley in the graph of a quantity (i.e. magnetic flux Φ, magnetic flux density B, field

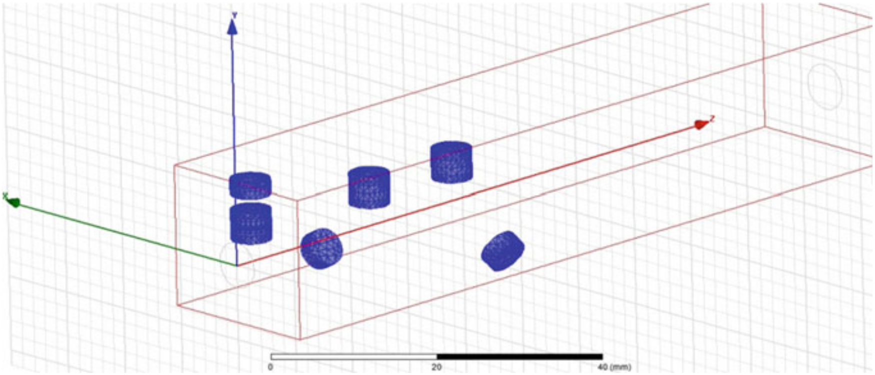

Fig. 5.1 A representative mesh structure

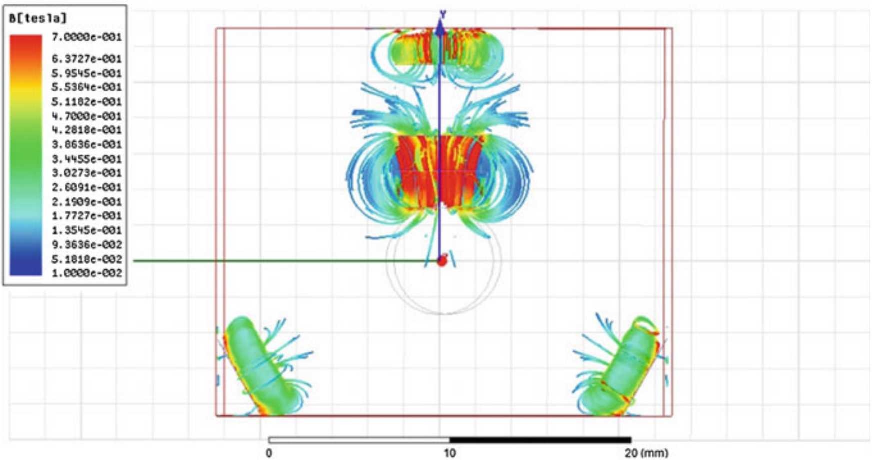

Fig. 5.2 A sample magnetostatic solution of a magnetic piezoelectric harvester

strength H, etc.) as function of number of mesh, then the left edge of this valley can be used for a proper mesh number [26].

The modeling of piezoelectric systems can be made as function of time by using Runge-Kutta time integration technique. It is a proper technique, since the fourth order term addiction gives good sensitivity for the estimation of quantities such as position, velocity, voltage, current, etc. [18]. In addition, the findings of Runge-Kutta technique can be directly used for the dynamic analyzes as in [18, 19]. In the following chapters, the applications of this technique will be given.

After the initial drawings of the model harvester system, magnetostatic analyses can be carried out. From magnetostatic solutions, the effects of magnetic sources, magnetic fields can be found in detail in 3D media (see for instance Fig. 5.2).

Note that the fields may increase at the vicinities of magnetic sources such as magnets up to $B = 1.1$ T. The advantage of the 3D magnetostatic solution is that it can give the field values at every solution region. Therefore the model can be re-drawn easily for the best result. While the distance to a magnetic source is adjusted, one should keep in mind that the piezoelectric beam should not be put closer to the source. Since the magnetic force extremely increases, it can break the beam. Thus the simulations can also give the resulting magnetic force in order to estimate the optimal distance and save the laboratory materials with that respect.

5.3 Experimental Techniques

The setups in the piezoelectric energy harvester labs can include different equipments from various research fields. Therefore experimental techniques may require scientists from different fields such as acoustics, physics, electrical and computer engineering. The equipments, which are frequently used in the harvester studies can be summarized as follows: Shaker, amplifier, laser displacement sensor and controller, data acquation card, PC, oscilloscope, signal generator, magnets.

Figure 5.3a–c shows the setup of piezoelectric shaker test. The shakers operate with an amplifier in order to boost the amplitude of the vibration as in Fig. 5.3a. The amplifier and the signal generator are used to excite the shaker for piezoelectric tests. In some setups, a special package programme is used to excite the shaker. It can be operated under a laptop and a specific frequency and amplitude can easily be

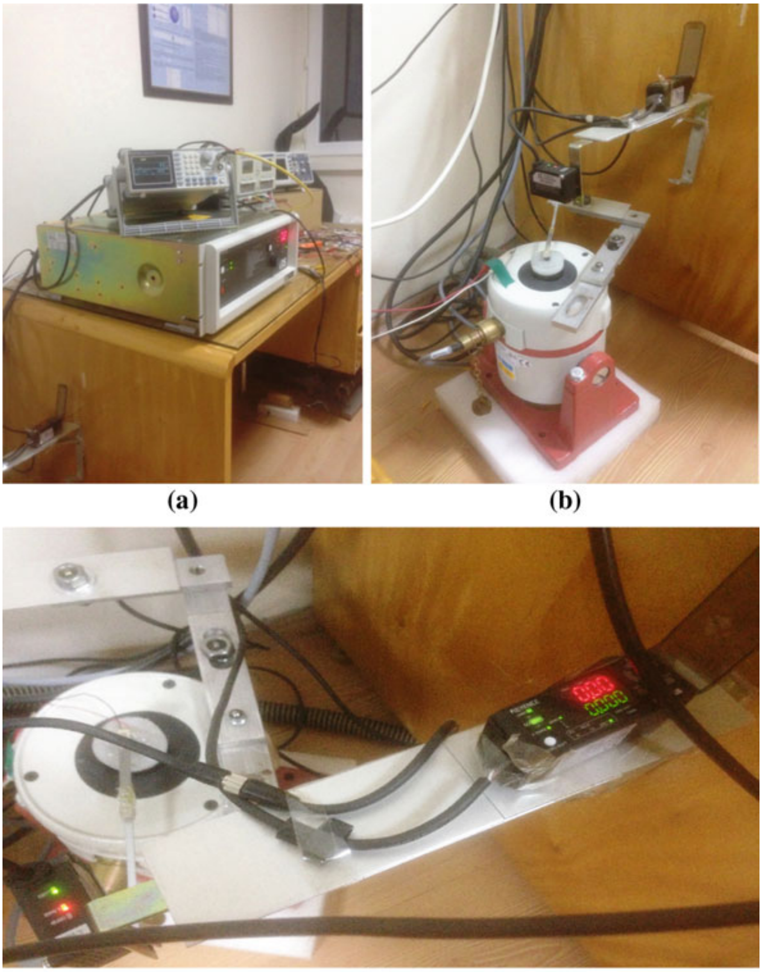

(a) (b)

(c)

Fig. 5.3 **a** The signal generator (*top*) and connected amplifier (*bottom*) for the excitation of shaker. **b** *Side view* of a shaker. **c** *Top view* of test equipment including a piezoelectric beam and the laser displacement sensor adjusted via the package and it does not require any signal generator. However it can increase the expenditures for such a setup. In Fig. 5.3b, c, the piezoelectric mounted shaker and the laser displacement sensor (black coloured) are seen on top of the system.

Indeed the excitation signal which comes from a signal generator with a certain frequency (generally 1–50 Hz) and amplitude (lower than 1 V peak to peak) is increased in amplitude and directed to the shaker to produce certain displacements at the tip of the piezoelectric beam. The vibration displacement can be adjusted by the amplifier just by increasing the output amplitude. However, if a certain frequency region will be sweeped, the amplitude should be constant for the experimental sensitivity. Because any small increase or decrease in displacement at the beam tip yields to different results, since the piezoelectrics are very sensitive to the buckling. The shaker setup can be used for the testing of frequency responses of the piezoelectric beams. When it vibrates the beam tip at certain frequencies f, the beam would produce fluctuations between the negative and positive sides of the equilibrium point. Figure 5.4 gives such a fluctuation on the laptop screen, if the fluctuations are read by the laser displacement sensor and send via a DAQ card.

For the interface of the laptop a LabView or other DAQ softwares can be used efficiently. It is possible with recent equipments that the laser displacement sensor and DAQ card can measure the vibrations with the sampling rate of 1 ms. This is a good accuracy in order to measure the higher frequencies of these kind of systems.

Figure 5.5 represents the results of a shaker test for three piezoelectric beams with various lengths. While the vibration amplitude of the long beam becomes large, the short one has small amplitude. In addition, the maximal amplitude, which

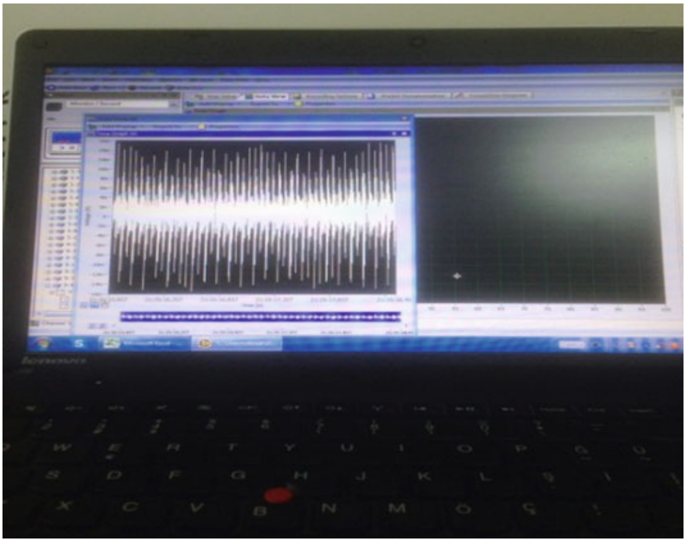

Fig. 5.4 Fluctuations of the piezoelectric beam at the shaker test

Fig. 5.5 Representative vibration amplitudes for three piezoelectric beams with various lengths: Long (*circle*), moderate (*square*) and short (*triangle*) from a shaker test

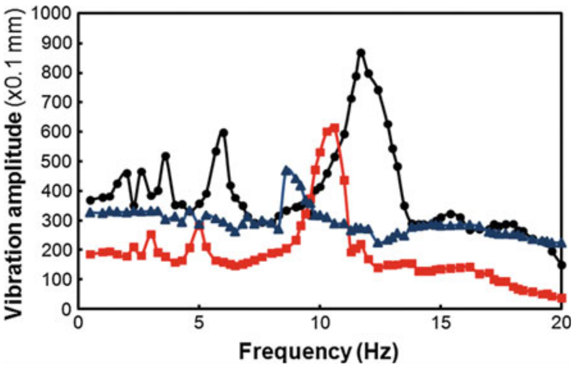

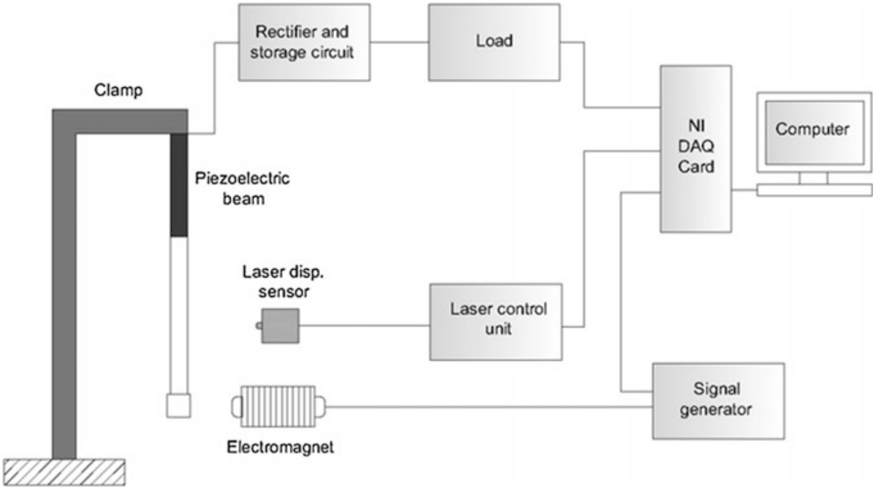

Fig. 5.6 The experimental diagram for the magnetic test system of a piezoelectric beam (*from* [27])

refers to the maximum power, is obtained for different frequencies. The reason is the difference in the natural frequencies of the beams due to their lengths. Similar to pendulums, the length will increase the period of the vibration and the f is decreased.

In order to test the harvesters in a magnetic media, the following setup has been proposed (Fig. 5.6). This system is different than the previous one, since there exists magnetic excitation in place of a mechanical one.

In this system, the response of the piezoelectric beam is tested for different magnetic excitation. The setup can give opportunity to adjust the strenght and the frequency of the magnetic field $\boldsymbol{B}$. The electromagnet is responsible to generate the

Table 5.2 The experimental parameters

Parameter	Symbol	Value
Force/voltage ratio	α	0.0001 N/V
Pendulum mass	m	27.4 g
Piezoelastic layer mass	m_p	10 g
Magnetic force coefficient	F_0	2750
Magnetic force coefficient	F_1	1500
Elastic stiffness coefficient	k	33.435 N/m
Piezoelastic layer capacitance	C	232 nF
Damping ratio	γ	1.48
Inductance of electromagnet coil	L	125 mH
Resistance of electromagnet coil	R_c	5.9 Ω

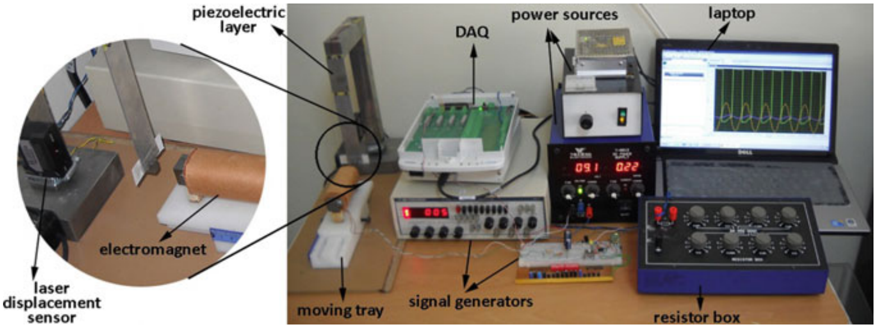

Fig. 5.7 The test setup under periodic field. From *left* to *right*, piezoelectric and non-ferromagnetic beam, laser displacement sensor, electromagnet, DAQ card, signal generator, electromagnet and LDS feeding sources, laptop and variable resistive loads

periodic $\boldsymbol{B}$. The distance of electromagnet to the tip of the beam is important, because the magnetic force strictly depends on the distance. The laser displacement sensor, DAQ Card, rectifier and storage circuit and signal generator are the main test equipments. Table 5.2 gives the experimental parameters of the equipments. In order to create a mathematical expression on the magnetic field effect, the waveform of the applied signal to the electromagnet is important. Such a problem will be introduced in Sect. 5.5. The vibration amplitude and the distance are given by $x(t)$ and d, respectively. Note also that a non-ferromagnetic beam is adhered to the piezoelectric beam tip in order to construct the desired length. The overall setup is shown in Fig. 5.7.

More than 500 thousand data points can be captured per second by the card in this setup. All experimental outputs are gathered by the LabView software. To determine the responses of harvester at different distances d to electromagnet, an adjustable slide mechanism is utilized, thereby the electromagnet can be moved forward and backward with respect to the beam tip. Throught the tests, input voltages for the electromagnet can be sweeped between 6 and 10 V in order to change the magnetic force $F_m(t)$. Note that the voltage directly influences the current on the electromagnet. Since the electromagnet is an inductive load (X_L), the resulting waveform can change (see Sect. 5.5). The magnetic periodic force is characterized as function of current I_c and the position of the piezoelectric layer tip u.

According to the test system, piezoelectric beam (sizes of 70 × 32 × 1.5 mm and the weight of 10 g) produced by Piezo System Inc is used. The capacitance and stiffness values of piezo-material are 232 nF and 188 N/m, respectively. The laser displacement sensor has a IL-065 type head and a IL-1000 control unit made by Keyence Inc. A rectifier and a storage circuit, a square pulse signal generating circuit, and an NI USB-6250 DAQ unit are also included. The magnetic excitation unit- the electromagnet has 1050 turns with 0.7 cm diameter copper wire. A ferromagnetic core (sizes of 120 × 20 × 20 mm and the relative permeability of μ_r = 10,000) is used to increase the field density. The laser displacement sensor which measures the vibration amplitude of the tip has a sensitivity of 4 µm. It is possible to get multiple records of different physical parameters such as vibration amplitude and harvested voltages in the experiments, synchronously.

5.4 Basic Methods of Nonlinear Analyses

The nonlinearity in engineering systems is important in the sense that the time-dependent systems can be out of stability by slight change in system parameters. Thus the estimated behavior cannot be observed and even it may affect the overall results. Even in many systems such as converters [28, 29], RL-diode circuits [30, 31], beams [19] the system can come out the controlled state and the behavior of the physical quantities such as position, velocity, voltage, amplitude, current, etc. becomes of randomized. Indeed the time-dependent change in these quantities may lead to unpredictable values or periodic states with higher harmonics. At that point, one requires a brief explanation on what the nonlinearity is. Figure 5.8 shows some quantities as function of a variable.

Fig. 5.8 Linearity and nonlinearity of the quantities

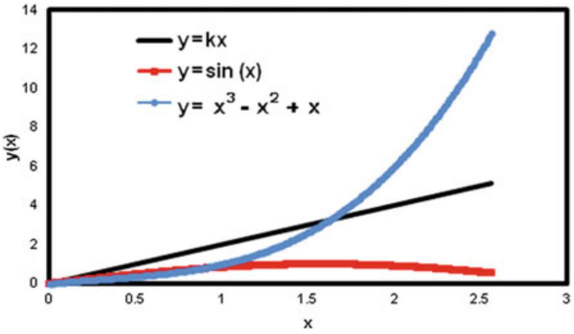

While the line gives a linear behavior with respect to the variable (i.e. x-axis), other two curves show complicated responses. Strictly speaking, the increase of x-axis does not yield to simple linear formula (i.e. $f(x) = ax$), indeed it may have higher order dependences to variable x such as x^2, $-x^3$, e^x, $Sin(x)$, etc. A small increase can yield to different results in $f(x)$ function, thereby all these functions are called as *nonlinear* [19, 32]. In many harvester systems, the quantities such as force, voltage, magnetic field indicate such a behavior.

There exist many tools to examine the results of a dynamic piezoelectric system. The following parts give explanations on these tools:

(a) **Phase Space Construction (Attractor Formation)**: In any higher dimensional system (i.e. higher than 1 variable), one can create a graph by putting one of the variables to the x-axis and the other to the y-axis. This representation simply gives the relation between these two variables (i.e. quantities) simultaneously. Thus, if these variables have a closed well-defined curve in the phase space representation, then one can identify the dynamics as "periodic". Indeed a periodic variable can have 2, 3 or more closed curves, then the periodicity is called such as 2P, 3P, etc. by giving a few different frequency in the variable. Figure 5.9 shows such an example.

If the phase space has no well-defined trajectory, indeed the output is assigned as "irregular". In such an attractor, the phase space fulls of many points and their position always changes by time by filling the certain region of the phase space. Beyond the quasi-periodic regime, these kinds of attractors are encountered frequently and those are the indicator of strong unpredictability. On the other hand, this irregular change in the variable is called as "chaotic". A representative example of such an attractor is shown in Fig. 5.10.

At first glance, the response of a dynamical system can be interpreted by forming the attractors, easily. It is easy since there exists a fundamental difference between Figs. 5.9 and 5.10 and it really helps to get an idea on the dynamic regimes.

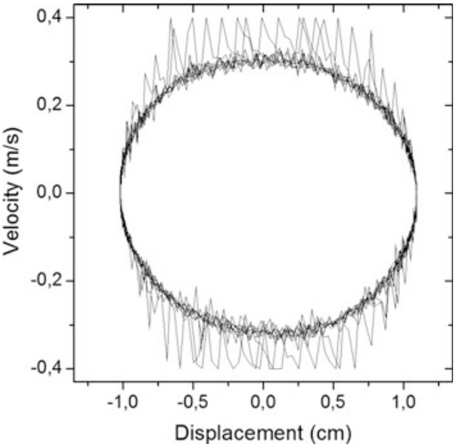

Fig. 5.9 Periodic phase space attractor from the regular motion of a piezoelectric beam

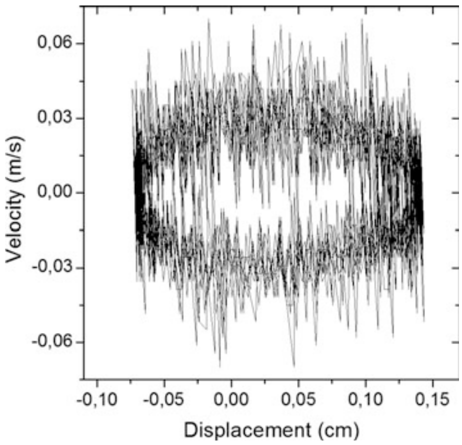

Fig. 5.10 Chaotic phase space attractor from the irregular motion of a piezoelectric beam

(b) **FFT Analysis**: Fast Fourier Transform (FFT) is very-well known process on the signal or image processing problems. It also finds broad application area in power electronics, since the harmonics, sub-harmonics and super-harmonics have importance on the design of a power electronics device. Indeed the dynamics of an output from any system variable can be analyzed by FFT and the frequency spectra can be identified in detail. From the analyses on the piezoelectric beams, periodic, quasi-periodic or chaotic spectrum can be easily understood. Mainly a chaotic output yields to a wide frequency spectra. It means that the output has the combination of many individual frequencies. Some of them can be larger than the main frequency f_0, some others can be smaller than f_0. Many peaks in the FFT indicate the chaotic output of the studied variables. On the other hand, the periodic output gives a basic FFT. A main peak and a few frequencies (they can be sub- or super- harmonics). Note that the peaks in a periodic FFT form can easily be identified, indeed it does not become complicated. Figure 5.11a, b shows two experimental examples on the FFTs from a piezoelectric beam.

(c) **Estimation of Lyapunov Exponents**: Lyapunov exponents determine the distance of the successive trajectories for a certain time evaluation in the phase space [33]. It mainly considers the exponential difference from an initial state for the system variables. Therefore the exponential change may increase the distances of future successive trajectories or it may decrease it. Therefore the logarithm of the ratio of the distances gives an idea how the variables improve in the phase space. The expression,

$$\lambda = \frac{1}{t_n - t_0} \sum_{i=1}^{n} \log_2 \frac{d(t_i)}{d(t_{i-1})} \tag{5.1}$$

gives the fastest growing exponential from the previous state. Indeed, there exist same numbers of exponential with the system variables. If the harvester

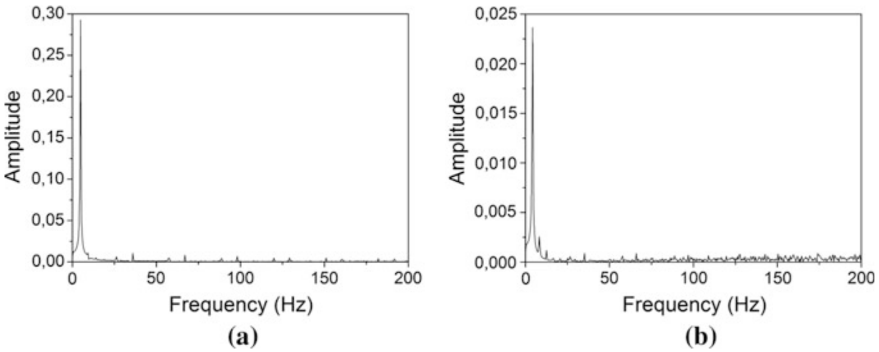

Fig. 5.11 Representative FFT analysis of a regular (**a**) and a chaotic (**b**) output

system has for instance, a coupled model of position, velocity and current as function of time, it means that it has 3 exponentials for each variable. However, the maximal exponential, which drives the overall system, is accepted as the maximal Lyapunov exponent and it is responsible for the future of the system trajectories. Note that if λ becomes negative, the trajectories get closer by time, however if it is positive, the trajectories move away.

5.5 Nonlinear Analysis of the Piezoelectric Harvester Systems

In this section, the nonlinear modeling procedure of some piezoelectric pendulum system under the changeable magnetic field is explained. In our previous study (see [19]), it was found that the vibrations of pendulum structures yield to many complicated responses. Indeed, the elasticity, the magnetic field strength, distance to the field source play important role to identify the dynamics. Initially, the pendulum model under the periodic external field is considered. The model of the setup in is given in Fig. 5.12.

In this model, it is considered that the electromagnet generates a pulsed magnetic field near the tip of beam. It has been known [19, 32] that the electromagnet can create a static and inhomogeneous magnetic field near the tip of the beam. Therefore, dynamics of the beam tip would include the elastic, gravitational and magnetic forces. In the considered system, the elastic force is much higher than the gravitational force since the mass of the system is small. With that respect, the effects of elastic and magnetic forces can be considered dominantly [19, 32, 34]. All forces which affect the tip can be summarized as in Fig. 5.13.

Following our studies [19, 27, 32] the forces in Fig. 5.13 gives the system equations. When the displacement $x(t)$ occurs at the tip of the pendulum, it produces

Fig. 5.12 The model of the piezoelectric pendulum in Fig. 5.7 (*from* [27])

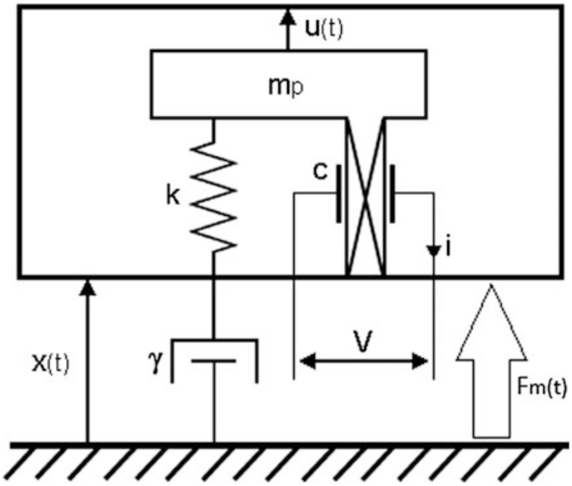

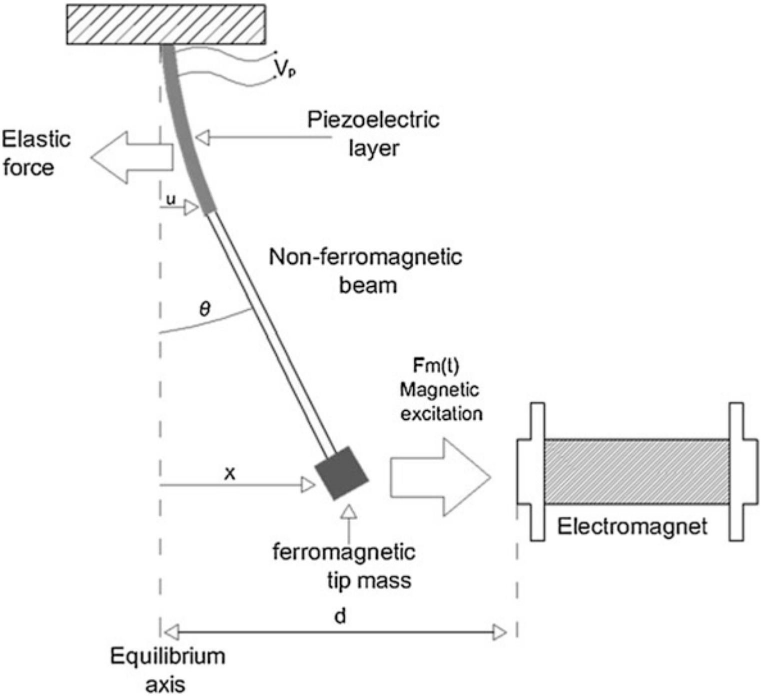

Fig. 5.13 The forces acting on the beam near the electromagnet

and internal mass displacement $u(t)$ inside the piezoelectric material. Here, Figs. 5.12 and 5.13 describe the system as a mass-spring, a damper and a capacitor. In this system, the rigid mass m_p and the stiffness constant k defines the mechanical property under a damper γ which denotes the mechanical losses. When the mass displacement u occurs in the layer, current I and voltage V are generated. In this case, the system equations is given by,

$$\begin{aligned} F_{total}(t) &= ku(t) + \alpha V(t) + F_m(t) \\ I(t) &= \alpha \frac{du(t)}{dt} - C\frac{dV(t)}{dt} \end{aligned} \tag{5.2}$$

Note that the equations include the mechanical and electrical parts. Here, the backward piezoelectric coupling is also included in addition to the mechanical effects. While C is the clamped capacitance, α denotes the force factor. If the displacement of mass inside the piezoelectrics u'(t) and the pendulum tip displacement x'(t) are used before the dimensionless form,

$$(m + m_p)\frac{d^2x'(t)}{dt'^2} = -\gamma\frac{du'(t)}{dt'} - m_p\frac{d^2u'(t)}{dt'^2} - ku'(t) - \alpha V(t) - F_m(t) \tag{5.3}$$

Here, the pendulum and piezoelectric beam masses are denoted by m and m_p, respectively. Considering the periodic magnetic force F_m(t), the equations can be written explicitly as follows:

$$\begin{aligned} &\frac{d^2x'(t)}{dt'^2} = -\frac{\gamma}{(m + m_p)}\frac{du'(t)}{dt'} - \frac{m_p}{(m + m_p)}\frac{d^2u'(t)}{dt'^2} - \frac{ku'(t)}{(m + m_p)} - \frac{\alpha V(t)}{(m + m_p)} - \frac{F_m(t)}{(m + m_p)} \\ &\frac{dV'(t)}{dt'} = \frac{\alpha}{C}\frac{du'(t)}{dt'} - \frac{I(t)}{C} \end{aligned} \tag{5.4}$$

Since x' is measured as 3 times of the displacement u', experimentally (see in Fig. 5.8), $u' = 0.33x'$ can be written. Then one arrives at,

$$\begin{aligned} \frac{d^2u'(t)}{dt'^2} &= -\frac{\gamma}{3m + 4m_p}\frac{du'(t)}{dt'} - \frac{k\,u'(t)}{3m + 4m_p} - \frac{\alpha\,V(t)}{3m + 4m_p} - \frac{F_m(t)}{3m + 4m_p} \\ \frac{dV'(t)}{dt'} &= \frac{\alpha}{C}\frac{du'(t)}{dt'} - \frac{I(t)}{C} \end{aligned} \tag{5.5}$$

The dimensionless form can be obtained when $t' = \tau t$, $y' = yd/\tau$, $u' = ud$ and $V' = V_0 V$ are introduced for time, velocity, position and voltage scaling, respectively. Note that τ determines the natural period of the pendulum and cannot be confused by the excitation period of the magnetic field T. Besides, to avoid the misunderstandings, d in later two expressions refers to the distance between the equilibrium point of pendulum and the tip of electromagnet. Then the dimensionless form can be written as;

$$\begin{aligned}
\frac{du}{dt} &= y \\
\frac{dy}{dt} &= -\frac{\gamma\tau}{3m+4m_p}y - \frac{k\tau^2}{3m+4m_p}u - \frac{(m+m_p)\tau^2 F_m(t)}{(3m+4m_p)d} - V\frac{\alpha\tau^2 V_0}{(3m+4m_p)d} \\
\frac{dV}{dt} &= \frac{\alpha d}{CV_0}\frac{du}{dt} - \frac{\tau V}{V_0 C R_L}
\end{aligned} \tag{5.6}$$

In above expression, d transfers the coordinate system into the equilibrium point of the beam. The vibration amplitude of the tip is represented by u.

The main problem is to find out the expression of magnetic force. The best way to find out the magnetic force expression, a magnetostatic analysis as similar to the case in Ref. [27] should be realized. The field lines are shown in Fig. 5.14 at the vicinity of the tip. Here, the *Poisson SuperFish* simulation package is used with FEM. The magnetic force F_m increases near the electromagnet and affects the ferromagnetic tip, dominantly. Flux density B decreases with the distance, thereby the 2D simulation can find the effect of the distance.

Figure 5.15 presents the results of the magnetostatic simulations. It has been found that these variations can be fitted to a combined function depending on the variables of u, U_c (i.e. I_c) and t. By considering Fig. 5.16, the overall nonlinear expression can be considered as the functions of electromagnet voltage U_c and the distance u,

$$F_m(t) = f_m(u) f_m(U_c, t) \tag{5.7}$$

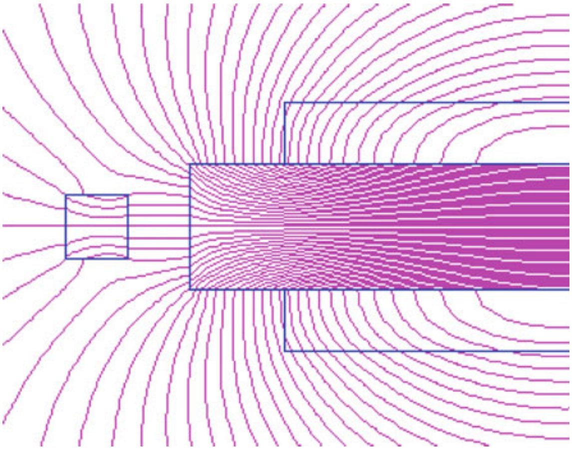

Fig. 5.14 The field lines at the vicinity of beam tip

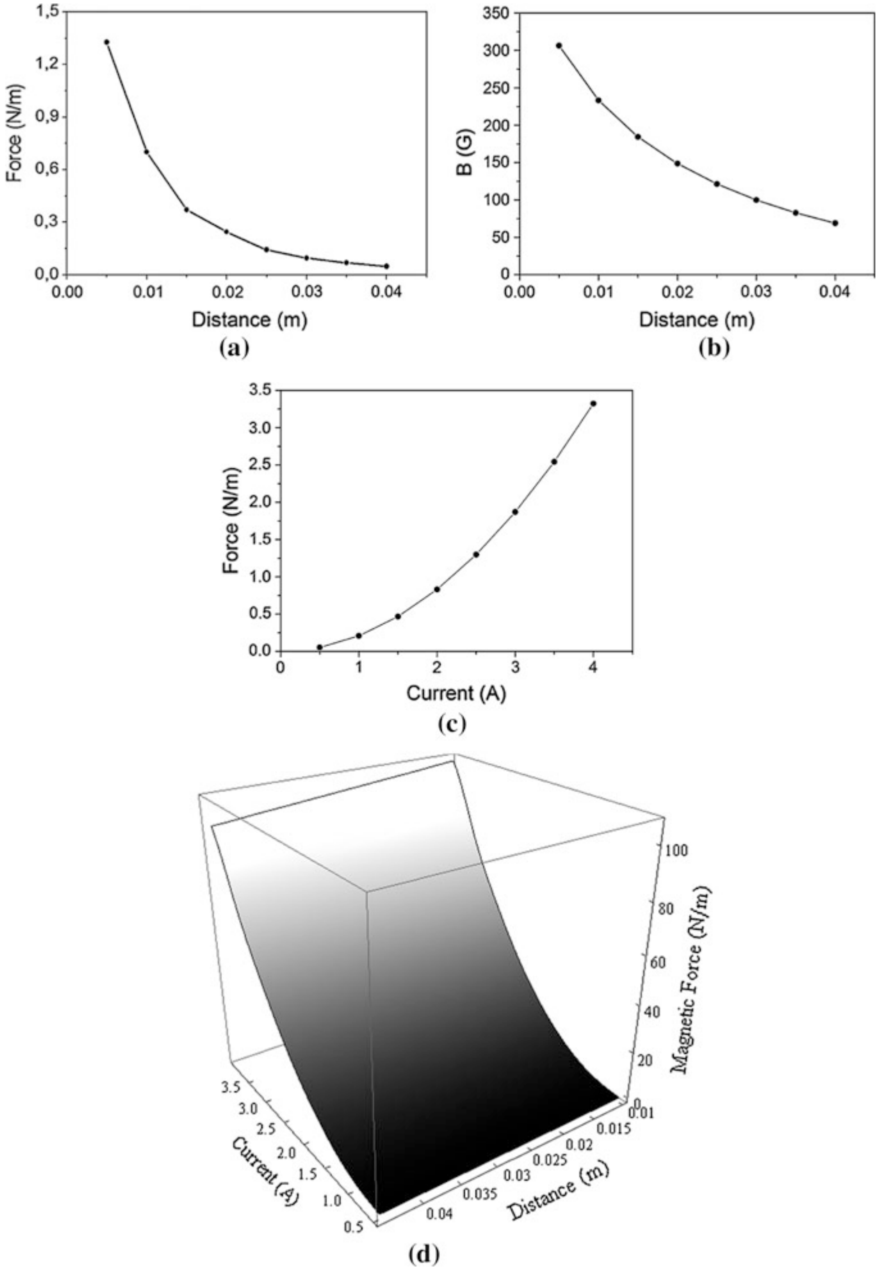

Fig. 5.15 Results of magnetostatic simulations: **a** Force, **b** magnetic flux density *B*, **c** force as function of the distance between the pendulum tip and electromagnet and **d** force on the plane of current and distance

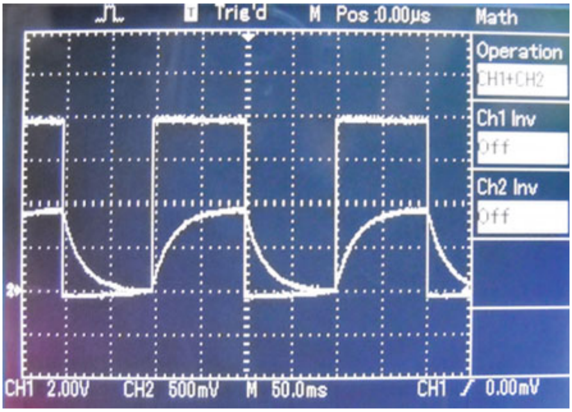

Fig. 5.16 Applied voltage to electromagnet terminals and the electromagnet current waveform which exerts the magnetic force

Note that the third-order polynomial function can fit better as in Ref. [18]. Since *$f_m(U_c,t)$* is the function of time due to the periodic excitation as seen in Fig. 5.16, the exponential functions appear as follows:

$$F_m(x) = \left\{ \begin{array}{ll} \left\{(1-0.7056/d)+0.0623(1-3u)+28026d(1-3u)^2-10^6d^2(1-3u)^3\right\} & \\ \left\{\alpha\left(\frac{U_c}{R_c}(1-e^{-R_c t/L})\right)^2-\beta\frac{U_c}{R_c}(1-e^{-R_c t/L})\right\} & 0<t\leq\frac{T}{2} \\ \left\{(1-0.7056/d)+0.0623(1-3u)+28026d(1-3u)^2-10^6d^2(1-3u)^3\right\} & \\ \left\{\alpha\left(\frac{U_c}{R_c}e^{-R_c t/L}\right)^2-\beta\frac{U_c}{R_c}e^{-R_c t/L}\right\} & \frac{T}{2}<t\leq T \end{array} \right\} \tag{5.8}$$

Here, d, U_c, R_c, L indicate the distance from the electromagnet to the pendulum equilibrium, voltage, resistance and inductance of the electromagnet coil, respectively. In the expression, the electromagnet force constants are defined as $\alpha = 8 \times 10^{-8}$ and $\beta = 10^{-9}$ from the electromagnetic simulation.

In order to simulate Eq. 5.6, the fourth order Runge-Kutta method can be used efficiently in the MatLab media. In that case, the time dependent results for position, velocity and voltage can be obtained. The main task is to fit the parameters of model and experiment. For this reason, the responses of simulation should be compared by the experimental findings. Therefore the damped results (without the magnetic excitation) can be compared at first step to estimate the best parameter fit.

From these graphs (Fig. 5.17), the natural period and frequency are found as $\tau = 0.210$ s and $f_0 = 4.76$ Hz. In addition, the damping constant is $\gamma = 1.48$ and the ratio of elastic constant to mass is *k/m* = 894. With the help of these parameters, the simulations and experiments fit well. Moreover, this model can be used for finite field values with the excitation frequencies.

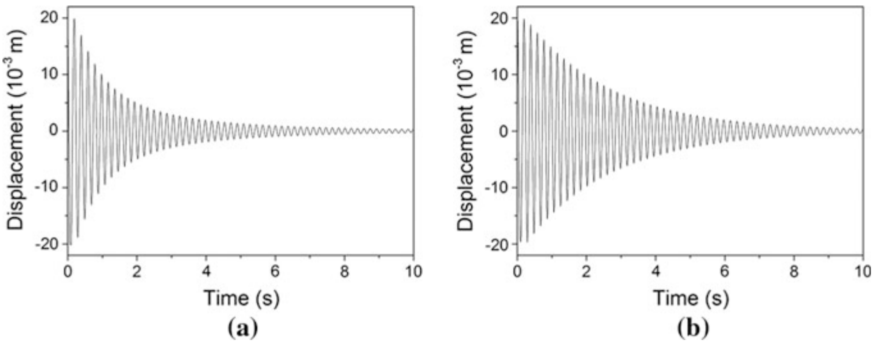

Fig. 5.17 **a** Experimental and **b** Theoretical vibration amplitudes *u* for non-magnetic case

In order to perform the averaged power output <*P*>, Eq. 5.6 is considered in frequency domain. While the second equation in Eq. 5.6 is written as,

$$V = \frac{jR_L \alpha \omega_m u}{1 + jCR_L \omega_m} \tag{5.9}$$

$$V = \frac{uR_L \alpha j \omega_m \left\{ (m + m_p)\, \omega_m^2 - F_0 < I_c^2 > + F_1 < I_c > \right\}}{(-\gamma j \omega_m - m_p \omega_m^2 - k)\,(1 + R_L C j \omega_m) - \alpha^2 R_L j \omega_m} + h.o.t. \tag{5.10}$$

Here the frequency ω_m is determined by the field. Note that the linear terms of the piezoelectric amplitude *u* is used in order to have an expression on power. Here $<I_c>$ and $<I_c^2>$ indicates the time-averaged values as below:

$$\begin{aligned} < I_c > &= \frac{V_c}{2R_c} + \frac{V_c L \omega_m}{2\pi R_c^2} \left(2e^{-\frac{R_c \pi}{L\omega_m}} - 1 - e^{-\frac{R_c 2\pi}{L\omega_m}} \right) \\ < I_c^2 > &= \frac{V_c^2}{2R_c^2} + \frac{V_c^2 L \omega_m}{4\pi R_c^3} \left(1 - e^{-\frac{R_c 4\pi}{L\omega_m}} \right) + \frac{L\omega_m}{\pi R_c} \left(e^{-\frac{R_c \pi}{L\omega_m}} - 1 \right) \end{aligned} \tag{5.11}$$

Here, the electrical parameters belong to the electromagnet coil. A certain voltage V_c with an excitation frequency of $\omega_m = 2\pi f$ is applied to the coil. Then, the power relation is found as follows:

$$< P > = \frac{u^2 R_L \alpha^2 \omega_m^2 \left\{ (m + m_p)\omega_m^2 - F_0 < I_c^2 > + F_1 < I_c > \right\}^2}{k^2(1 + C^2 R_L^2 \omega_m^2) + 2k\omega_m^2 (m_p + \alpha^2 C R_L^2 + C^2 m_p R_L^2 \omega_m^2) + \omega_m^2 \left\{ 2\alpha^2 \gamma R_L + \alpha^4 R_L^2 + 2\alpha^2 C m_p R_L^2 \omega_m^2 + \gamma^2 (1 + C^2 R_L^2 \omega_m^2) + m_p^2 \omega_m^2 (1 + C^2 R_L^2 \omega_m^2) \right\}} \tag{5.12}$$

The linear part of Eq. 5.8 as function of *u* and its complex conjugate divided by load resistance R_L, one arrives at $< P > = < VV^* > / R_L$. Equation 5.12 gives the relation between the output power and the electrical/mechanical parameters of the system. By using this formula, it is also possible to find out the optimal load resistance. If one gets the derivative of this equation with respect to R_L, the optimal

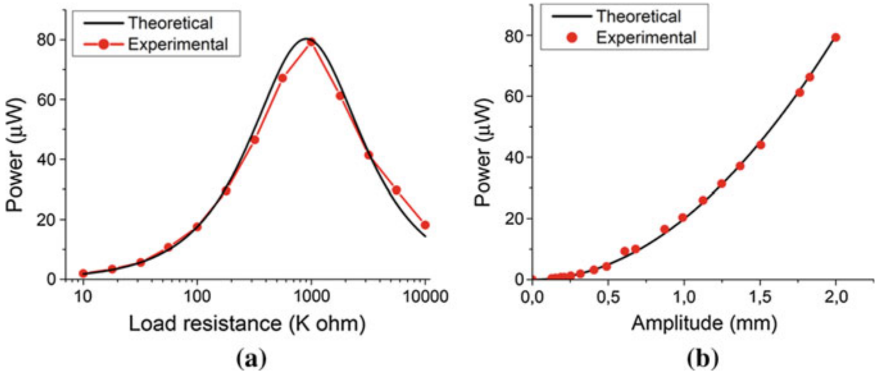

Fig. 5.18 The load resistance (**a**) and vibration amplitude (**b**) dependences of power. $d = 2$ cm and the voltage applied to the electromagnet terminals is 8 V [27]

load resistance is found as $(\omega C)^{-1}$. Here, ω and C give the frequency of magnetic field and the capacitance of the piezoelectric material, respectively.

Figure 5.18 gives the experimental and theoretical results of the averaged power. The resistive load about 1 MΩ gives the optimum power of the piezoelectric beam. As in other electrical systems, the piezoelectric beam gives the maximal power output when the load resistance equals to its internal empedance.

It is obvious that the theoretical and experimental explorations give the same value. In addition, power depends on the vibration amplitude with a higher order polynomial function (see in Fig. 5.18b). With higher deflactions, much power is obtained.

5.6 Experimental and Theoretical Results of Nonlinearity

In this part, the test results with respect to vibration amplitude, tip velocity and output voltage are discussed. Figure 5.19a–c presents the dynamic responses of the beam tip. It is understood that velocity has some ripples at the maximal values when the tip is at the equilibrium point. The output voltage is not ideal sinusoidal, however it has the same phase with the velocity. In Fig. 5.19d the phase plane trajectories give ripples at minimal and maximal points of velocity as stated before. This phase space representation shows these ripples much clear. Since an ideal periodic motion yields to a simple circle or ellipse in the phase space, the ripples here point out a non-regular dynamics even at the natural frequency of the system.

It has been proven that these ripples are resulted by the magnetic field [27]. The ripples cannot be related to any noisy data, because the external magnetic excitation is very strong for the adjusted parameter set. Even in the theoretical formulation, it yields to similar ripples. The spectral analysis shows that there exist some high frequencies but low amplitude effects in the velocity data. It can have 88 Hz

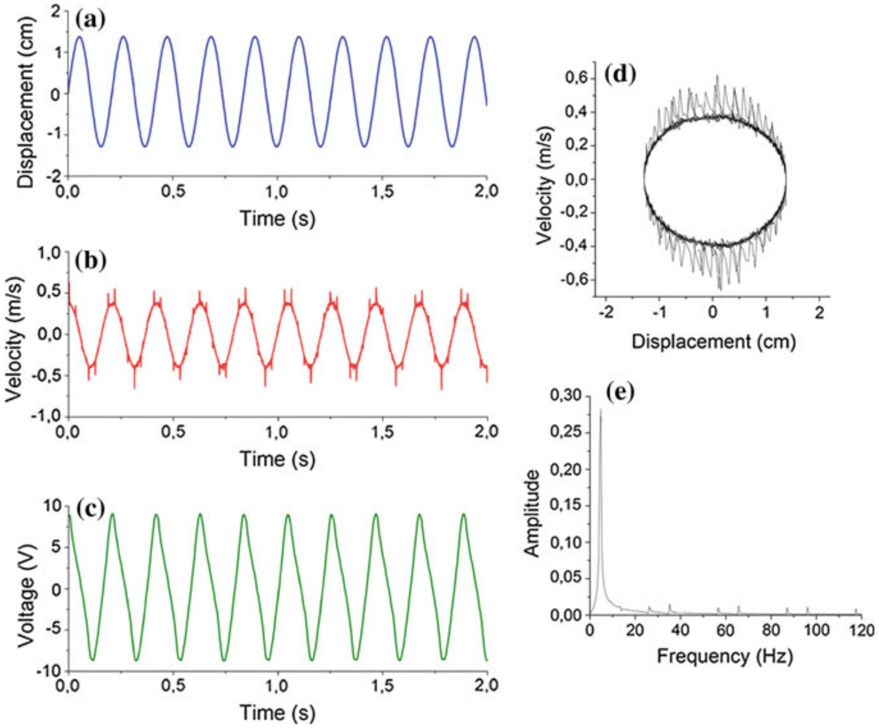

Fig. 5.19 Observation of **a** harvester tip displacement, **b** tip velocity, **c** voltage, **d** phase space portrait and **e** power spectrum of the velocity in the case $d = 2$ cm, $\omega_m = 4.76$ Hz, $R_L = 500$ kΩ

component and that explains the ripples occurring in a very short time scale. Strictly speaking, the main frequency 4.7 Hz and other high frequency components such as 14.6, 26.3, 34.9 and 56.3 Hz are clearly seen in the spectrum (Fig. 5.19e).

When the field frequency ω_m is increased to 6.09 Hz, the dynamics becomes much complicated (Fig. 5.20a). Both the velocity and voltage shows ripples as in Fig. 5.20b, c, however the vibration amplitude has still a sinusoidal character. In addition to the main frequency 6.09 Hz, there exist infinite numbers of frequencies in the spectrum as shown the inset of Fig. 5.20e. Some frequencies with larger amplitudes can be summarized as follows: 24, 36, 54, 156, 256, 425, 452 Hz etc.. These frequencies produce many ripples as in Fig. 5.20d and dominate the phase space. Thus the nonlinearity governs the dynamics for non-natural frequencies. On the other hand, these high frequencies such as 425 and 452 Hz in the velocity data are observed first time, experimentally in such a large-scale piezoelectric system to our knowledge. This result proves how the nonlinearity is important for such harvester systems and encourages us to obtain better power solutions for magnetically excited systems. Although the vibration amplitude becomes sinusoidal, the wide-band structure in velocity causes smooth power decay for different excitation frequencies as will be shown later.

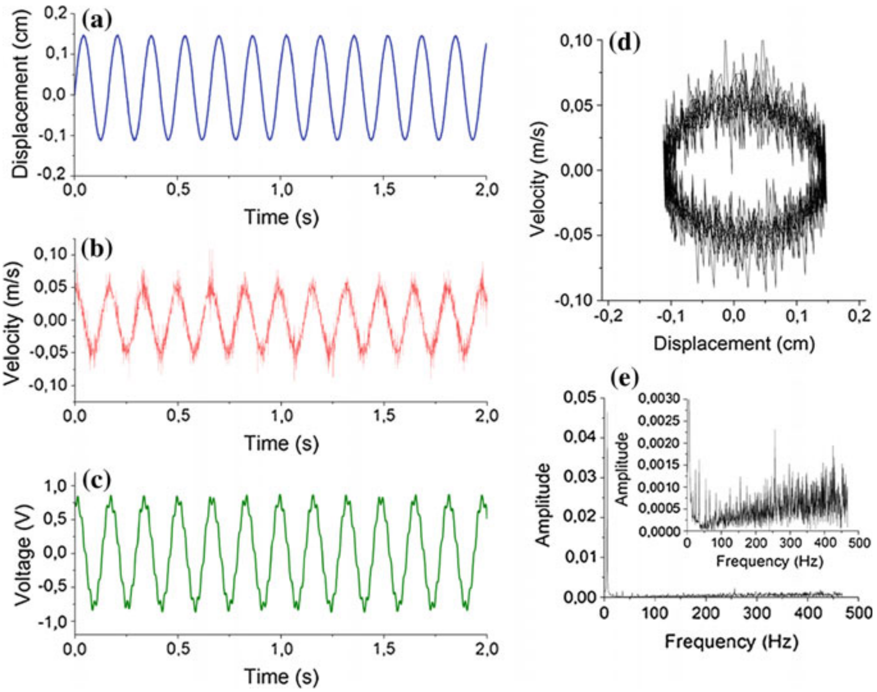

Fig. 5.20 The experimental results of **a** harvester tip displacement, **b** tip velocity, **c** voltage, **d** phase space portrait and **e** power spectrum of the velocity in the case $d = 2$ cm, $\omega_m = 6.09$ Hz, $R_L = 500$ kΩ

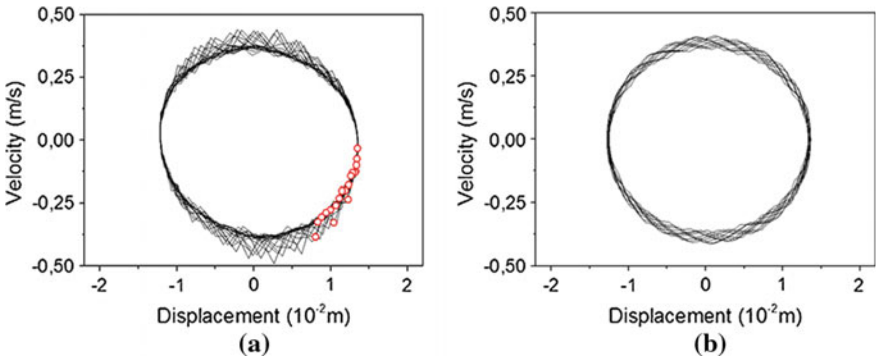

Fig. 5.21 Experimental (**a**) and theoretical (**b**) attractors for $\omega_m = 4.76$ Hz and $d = 2$ cm. The points represent Poincare sections

Figure 5.21 represents the experimental and theoretical attractors for another experimental set. Note that the only change in this parameter set is the current over the electromagnet (i.e. lower magnetic force). The ripples still exist, however their

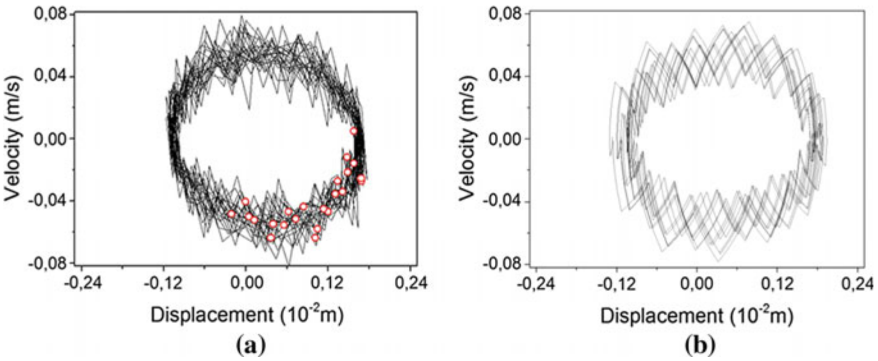

Fig. 5.22 Experimental (**a**) and theoretical (**b**) attractors for ω_m = 6.02 Hz. The points represent Poincare sections [18]

lengths are low compared to the case in Fig. 5.19. The open circles on the experimental data gives the Poincare section data, which is separated on the phase space after the same time interval. The theoretical attractor, which was calculated from Eq. 5.6 is shown in Fig. 5.21b and gives a good similarity to the experimental one.

The vibration amplitude of the beam tip becomes larger, when the field frequency approaches to the natural frequency of the system (i.e. $\omega_m = \omega_0$ = 4.76 Hz). Thus the frequencies near the natural frequency of the system are better to harvest much energy from the system, since the voltage generated by the piezoelectric layer is found to be dependent on the vibration amplitude. In Fig. 5.22, the attractors of another parameter (i.e. ω_m = 6.02 Hz) are compared. The changeable character of the magnetic flux can be seen in velocity fluctuations dominantly, whereas the vibration amplitude gets smaller values compared to the earlier cases. The similarity persists again between the theoretical and experimental findings. Note also the distributed Poincare section points on the attractor in Fig. 5.22a.

In addition to the similarities between the model system and the experimental one, the harvester systems show another interesting phenomena called hardening and softening effects. In Fig. 5.23, an example of this strange hysteresis bahaviour is presented. Here, while the blue plot gives the maximal voltage when the excitation field frequency is increased up step by step, the red plot gives the maximal voltage when the frequency is decreased gradually.

The frequency increase causes a harvesting effect with small amplitudes around 5 V (as in sweep up case) as in Fig. 5.23. But the frequency lowering beyond the natural frequency causes three-fold voltage harvest in the softening effect. This behavior is the result of the piezoelectric layer type. While some layers indicate softening effect, others give hardening effect, where increasing frequency yields to high amplitudes. As a result of these hysteresis effects, the excitation frequency

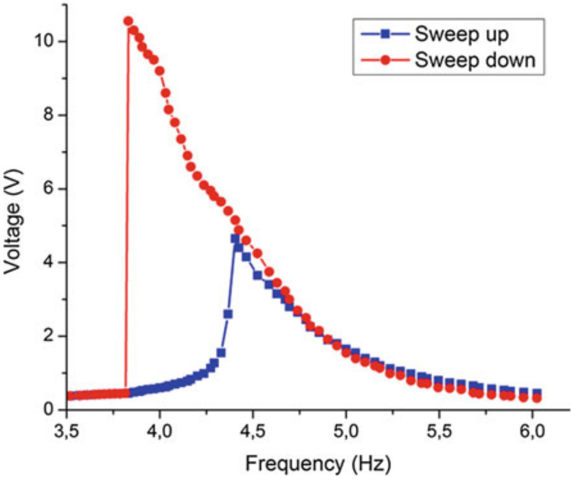

Fig. 5.23 Peak voltage as function of the excitation frequency ω_m. Softening effect is observed for the sweep up/down cases. The parameters are $d = 2$ cm, the load resistance $R_L = 820$ kΩ and the maximum voltage over electromagnet $U_c = 8$ V

should always change at the vicinity of natural frequency, where jumps in amplitudes can be observed.

5.7 The Dependence of Dynamics and Power to the System Parameters

In this section, the parametrical dependence of power in pendulum-like harvesters will be explained. For this aim, the dynamic feature of such a system can be summarized by an intuitive bifurcation diagram (Fig. 5.24). Indeed, such diagram can be produced by adjusting a parameter or two parameters on a plane. If one parameter dependency is studied, it is called one-dimensional bifurcation diagram, whereas two parameters are studied together on a parameter plane, it would be a two-dimensional bifurcation diagram. The bifurcation data can be produced by displacement, velocity or harvested voltage for successive parameter changes. Therefore it is nothing else than the collection of many Poincare sections. According to Fig. 5.24, the frequency values less than 4.8 Hz give regular displacement values and a periodic behavior is observed. However beyond this value, displacement values fluctuate between 0.4 and 1.4 cm till the excitation frequency becomes 5.1 Hz. The displacement vibrations become regular (i.e. periodic) for larger values. In the case of velocity (i.e. filled circles), the motion is much complicated since the fluctuations does not decay to a certain velocity value for any excitation frequency.

Fig. 5.24 The experimental bifurcation diagram ($d = 2$ cm, $U_c = 8$ V). The bifurcation parameter is magnetic field excitation frequency

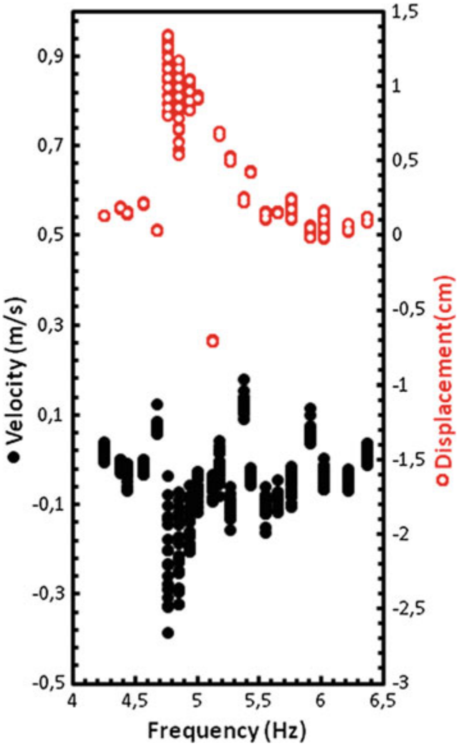

The parametrical dependencies can also be found by root mean square (RMS) data, which is given by [35]:

$$x_{rms} = \sqrt{\frac{1}{n}\left(x_1^2 + x_2^2 + \cdots + x_n^2\right)} \tag{5.13}$$

Displacement and velocity data are represented by x_n, and n gives the total data point. It is interesting that there exist a good relation between RMS values of data and the corresponding output power as in Fig. 5.25. Indeed, this relation can be found for both experimental and theoretical data. All data can be fitted to a second order formula, which states that power increases parabolically as function of displacement and velocity rms data.

This invention of this relation is new for magnetically-excited systems and it gives a very clear result, which enables one to estimate output power just by looking at rms data of displacement and velocity [18]. In Fig. 5.26, another interesting result is given. The RMS values of displacement and velocity enables us to determine the natural frequency of the harvester system. Both RMS displacement and velocity data jumps at natural frequency. In this experiment, the natural frequency is 4.76 Hz.

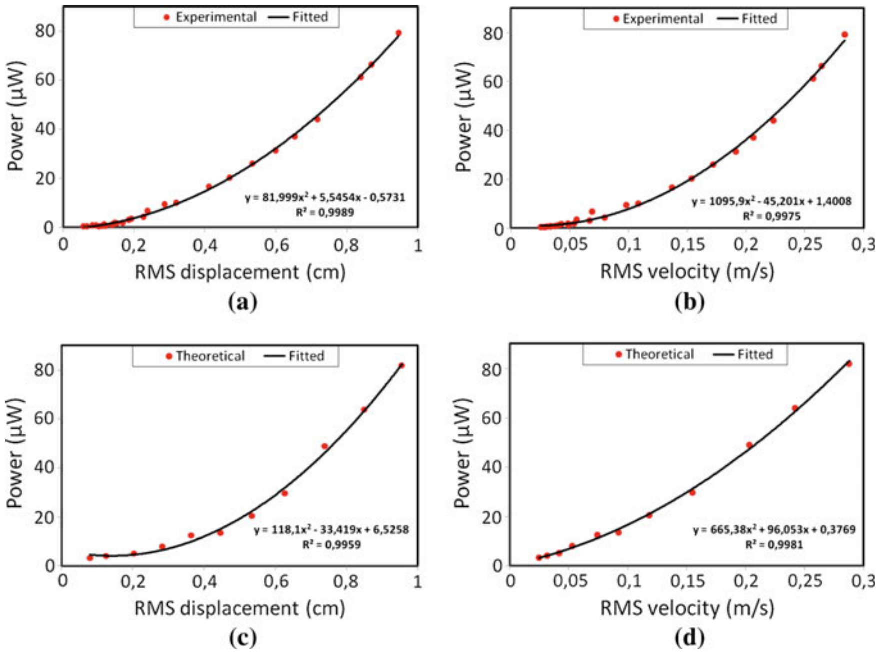

Fig. 5.25 Experimental (**a, b**) and theoretical (**c, d**) relation between displacement/velocity and output power. (d = 2 cm, U_c = 8 V and the frequency changes between 4.25 and 6.53 Hz.)

One of the important concepts to measure the nonlinearity of time-dependent data is the fluctuation amount. The nonlinearity of any fluctuation increases, when different frequencies are included in the data. When one gets the amplitudes of individual frequencies from the FFT result, a quantitative scaling can be obtained for the data. This process is mainly described with the concept of total harmonic distortion (THD) [17, 36]:

$$THD = \frac{\sqrt{\sum_{i=1}^{N_f} A_i^2}}{A_0} \tag{5.14}$$

where A_0 denotes the main frequency of the displacement or velocity data. A_i and N_f denote other frequencies and the number of total frequencies in the FFT, respectively.

In Fig. 5.27a, b, the THD results of the data are presented as function of excitation frequency. It is obvious that displacement fluctuations are smoother than velocity fluctuations in Fig. 5.27b. The nonlinearity becomes 5 times powerful in velocity fluctuations for some f values compared to the displacement fluctuations.

Fig. 5.26 The dependence of rms position and velocity to the excitation frequency

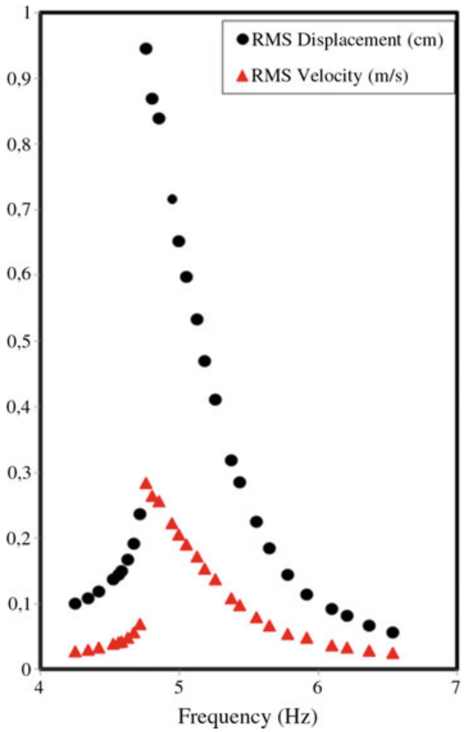

While the maximal distortions are obtained at lower f for both displacement and velocity, a contradiction occurs at the vicinity of natural frequency.

Because the distortion in displacement increases up to 6 at the vicinity of f_0, the distortion in velocity stays lower near 15 at the same frequency. Note also that there is a slightly decreasing character in THD of displacement (Fig. 5.27a). However, in the case of velocity, THD increases for higher frequencies as seen in Fig. 5.27b. Thus, these results prove that while the nonlinearity of displacement is generally higher for the frequencies lower than natural frequency of the system, the nonlinearity of the velocity stays higher for lower and higher frequencies and becomes lower at relatively medium frequencies. In order to find a relation between displacement/velocity THD values and output power, Fig. 5.28 is depicted. While the output power maximizes at $f = 4.8$ Hz, THD of velocity minimizes. Thus, it proves that the power decreases when irregularity increase in the velocity data. Whereas there is no significant correlation or anti-correlation between displacement and power.

From the electrical point of view, the resistive load R_L and excitation frequency f are important. In order to show this combined effect, Fig. 5.29 is presented.

There exists a certain maximum for specific resistance and magnetic excitation frequency. The output power of harvester becomes maximal, when f gets closer to the natural frequency. While the dependence on the frequency is much strict in

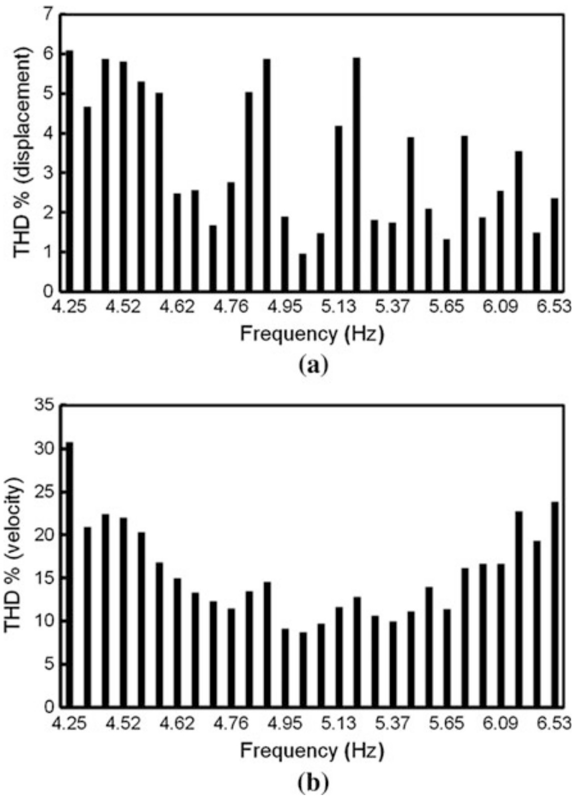

Fig. 5.27 The total harmonic distortion percentages (THD %) of **a** displacements and **b** velocities for excitation frequency

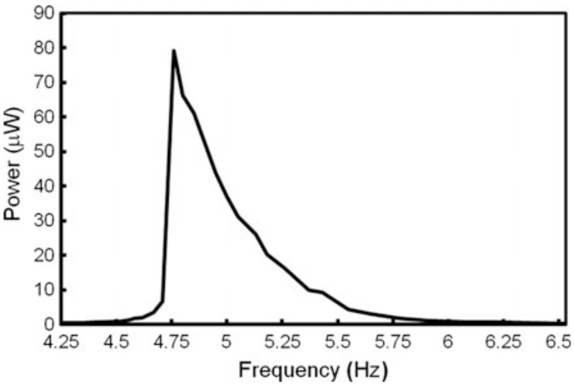

Fig. 5.28 The corresponding output power as function of excitation frequency

order to get the maximal output, the resistance dependence affects the output power relatively low. Note that the resistance axis is in the logarithmic scale. Another important result is that the harvester power shows the wider frequency region at its same value for the resistive loads of 1 MΩ. Thus if one requires much stable output for a wider range of excitation frequencies from the harvester, the load should be adjusted at that value otherwise the maximal output can be generated at certain parameters.

5.8 Maximal Power Point Tracking Techniques for Piezoelectric Harvesters

Parallel to the findings of previous section, a harvester gives the maximal power generation for a specific vibration frequency and load (see in Fig. 5.29). Therefore an efficient maximal power point tracking (MPPT) technique should be applied in order to get the optimized energy. In the literature there exist various techniques for the MPPT techniques [37–39]. Initially, it should be pointed out that surface mounted devices (SMD) can be preferable to decrease the power loss in the circuit

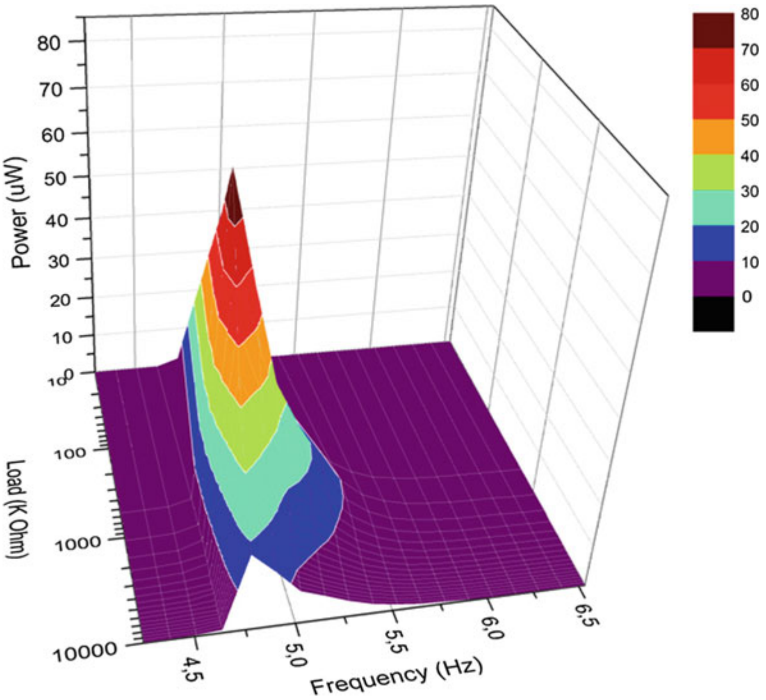

Fig. 5.29 Harvested power on the plane of resistive load and excitation frequency ω_m

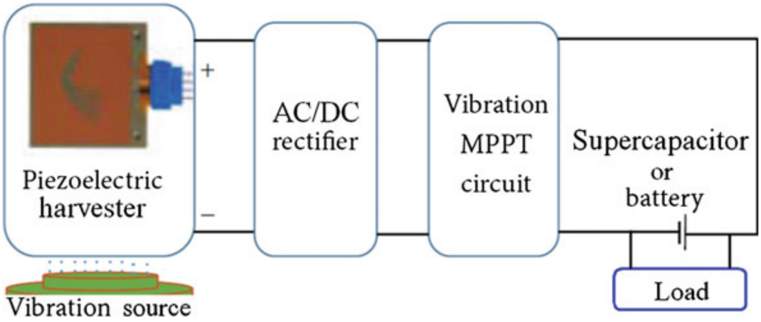

Fig. 5.30 The circuit diagram which enables to use of the harvested power: Rectification, storage and MPPT

elements since they generate μW or mW scale powers. Figure 5.30 shows a general circuit model with rectification, storage, MPPT and electrical load.

The harvested signal is initially rectified and transferred to an MPPT circuit just before the storage unit. Two recent MPPT techniques are mentioned below:

1. DC/DC single inductor dual output (SIDO) control technique,
2. The single-supply pre-biasing (SSPB) technique.

The SIDO control equipments and MPPT circuit diagram which are introduced by Ramond et al. [37] is shown in Fig. 5.31. After the harvester part in the left hand-side an AC/DC recitifier is first used as also refered in Fig. 5.30. Later, the MPPT and controller part is added to the system for an optimized power control. In the MPPT part of Fig. 5.31, there is a certain voltage value called VMPP for which the power PMPP is delivered maximal from the harvester. After this MPP, the power decreases by the voltage increase until it reaches a value VOC, the Open Circuit voltage of the harvester for which the harvested power is null. The main

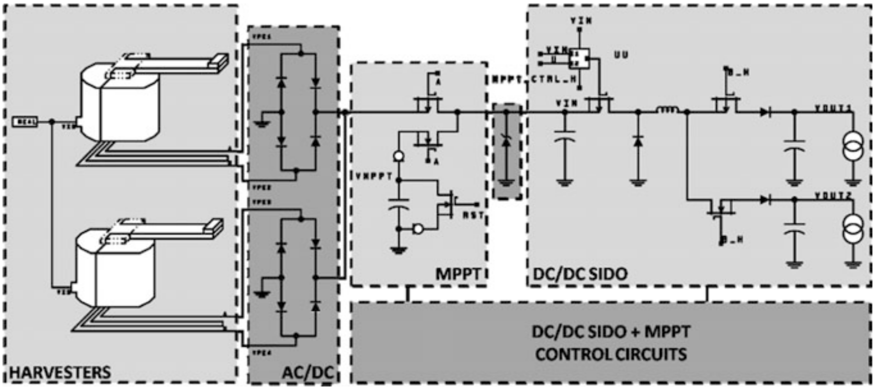

Fig. 5.31 The detailed connection of MPPT and DC/DC SIDO control circuit (*from* [37])

Table 5.3 Harvester characterization summary with SIDO control technique (*from* [37])

Vibration level (g)	$\lvert P_{MPP}\rvert$ [W]	$\lvert V_{MPP}\rvert$ [V]	$\lvert V_{OC}\rvert$ [V]	$\lvert V_{OC}\rvert/\lvert V_{MPP}\rvert$
0.1	3.5×10^{-6}	1.26	2.10	0.6
0.3	35.5×10^{-6}	4.02	6.77	0.59
0.5	103×10^{-6}	6.83	11.48	0.59

function of this MPPT technique is to sample the open circuit voltage of the harvester, periodically in order to provide a reference voltage to the DC/DC converter. Indeed as shown in Table 5.3, the ratio VMPP/VOC is constant over the whole vibration level range (0.1–0.5 g). Thus the DC/DC converter regulates the harvester polarization voltage around VMPP leading to a maximal power emission with an average efficiency of 95%.

Consequently in order to achieve an optimal power, the micropower management system should regulate the voltage of the harvester and place it close to the MPP. According to literature, this kind of MPPT problem has been solved using the charge pump or inductive DC/DC converters in order to isolate the piezoelectric layer from heavy electrical load and enable to control the polarization of the source independently of the load voltage (Fig. 5.32a). The solutions proposed by Yi et al. [40] and Simjee and Chou [41] are interesting but all the power consumed by the

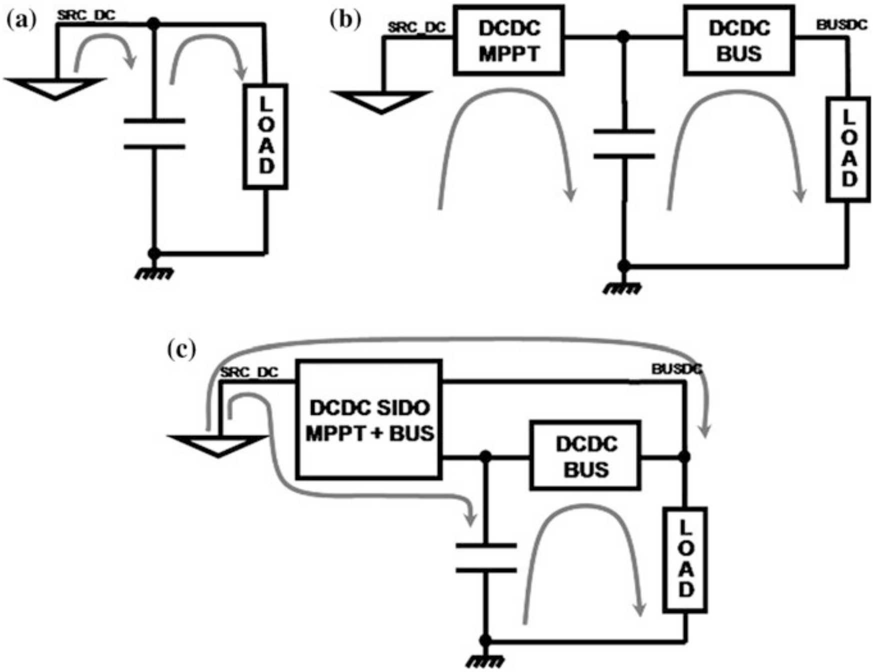

Fig. 5.32 Various MPPT management systems in the literature (*from* [37])

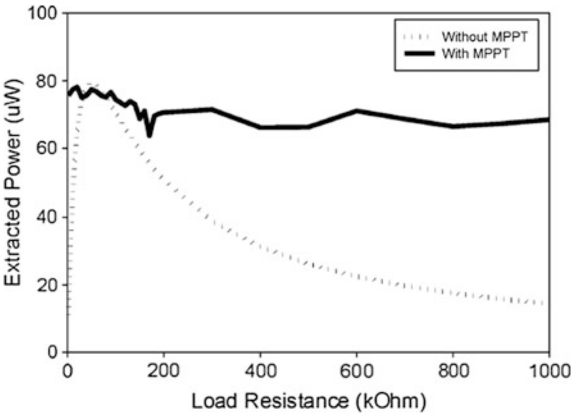

Fig. 5.33 The harvested power with/without MPPT from a piezoelectric layer (*from* [42])

load passes through the storage element and two converters (see in Fig. 5.32b), which decrease the overall efficiency of the system.

Figure 5.32c proposes another MPPT solution by providing a high efficiency direct power path from the source to the load in addition to the MPPT scheme by using a Single Inductor Dual Output (SIDO) DC/DC converter. The MPPT system operates with the control circuit as in Fig. 5.31 as well. According to the findings of Do et al. [42], the effect of an MPPT system can be seen in Fig. 5.33.

The bell-shaped dotted curve shows the harvested power after the rectifier for various ohmic loads. For the high loads then 200 kΩ, there exists a dramatical decrease in power as also shown in Fig. 5.29 in the previous section. However, the MPPT system produces a much rough output for high loads and the output power is nearly fixed around 70 μW.

Other recently proposed MPPT technique is called as single-supply pre-biasing (SSPB). According to Elliott and Mitcheson [39], their technique enables the damping force to be set by a fixed voltage and by varying that voltage, real-time adaptation to variations in the mechanical force can be implemented.

Every half cycle of vibration, charge is placed on the piezoelectric material which will induce a force opposing the motion of the piezoelectric material. This tries to dampen the beam's motion, causing an increase in the harvested power. SSPB changes the circuit from a velocity-damped resonant generator (VDRG) to a Coulomb-damped resonant generator (CDRG) [43], enabling the level of damping applied to be readily set by the pre-bias voltage, V_{cc}. At the piezoelectric beam's extreme points, charge from the pre-biasing capacitor, C_{bias}, is transferred on to the beam. This generates a Coulomb force to oppose the beam's vibration until it reaches the opposite extreme position. The energy on the beam is then discharged back into $\mathrm{C_{bias}}$, and the process repeats. Similarly to the bridge rectifier, the damping force can be optimally set by setting the voltage on the storage device in order to achieve maximum power extraction,

$$P_{\max} = \frac{8Q}{\pi} V_{po}^2 f_0 C_p \quad \text{and it is applied when} \quad V_{opt} = 2V_{po}\frac{\gamma}{1-\gamma^2} \tag{5.15}$$

Here Q is the Q-factor of the resonant current discharge path through the inductor and is the fraction of the magnitude of the voltage conserved on the capacitor of an RLC oscillator with Q-factor after a half-cycle of the oscillator. The system must detect a change in the piezoelectric induced voltage, quantify the magnitude of the change, and operate an appropriate response. Since both the bridge rectifier and SSPB techniques use a voltage on a bias capacitor to apply the optimal conduction angle and damping force respectively, adding a buck converter with battery enables the bias capacitor voltage to be independently set. The MPPT scheme operates by adjusting the off-time of the buck converter causing the energy on the bias capacitor to be more or less frequently transferred, resulting in a decrease or increase in voltage respectively. Figure 5.34 shows the suggested topology to adjust the voltage applied for the SSPB circuit. The voltage on the biasing capacitor, C_{bias}, is controlled by varying the power transferred through the buck converter. If the time between energy transfers is increased, C_{bias} voltage would rise and a greater damping force is applied to the piezoelectric material. For the implementation of the SSPB technique, the system requires three elements [39]: A circuit to measure the harvested power, a controller to decide whether the power has increased or decreased object to the previous measurement and a buck converter to transfer the energy. In the design of these circuits, power consumption should be minimised for the highest efficiency. Figure 5.35 gives the implementation to demonstrate the MPPT technique.

The measurement and control circuitry should operate at the lowest voltage possible, but the voltage on the biasing capacitor maybe several times larger than this. A potential divider can also be used by switching in across the biasing capacitor during the operation (see in Fig. 5.35). The switch can be an n-type MOSFET (BSS138), which can be driven by a low power FPGA (Igloo Nano). It can also be used to implement the SSPB scheme [39]. A low power Analog-to-Digital Converter (ADC AD7468) can be used to measure the voltage and a Booth Multiplier algorithm [44] on the FPGA can square the value.

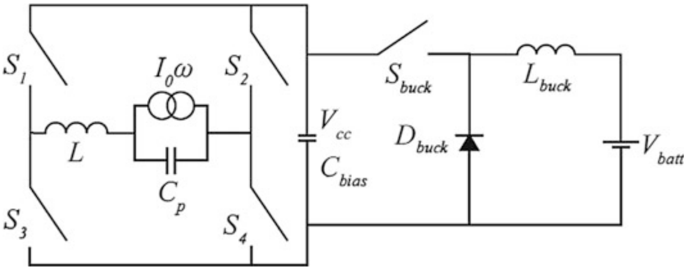

Fig. 5.34 The SSPB unit attached to a buck converter and battery (*from* [39])

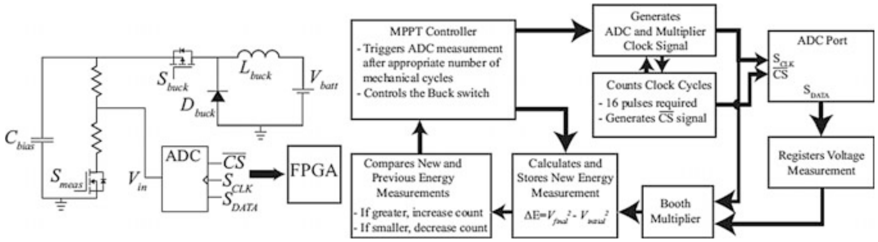

Fig. 5.35 SSPB MPPT implementation and controller (*from* [39])

5.9 Conclusions

In this chapter, the outlines of the dynamic explorations of the harvester systems have been explained. Mainly, the 3D system modeling, electromagnetic analyses and time-dependent simulations have been defined for the widely worked pendulum system. While the 3D modeling of the system gives a clue on the electromagnetic effects, especially the magnetic force steming from the permanent magnets or a stable curring carrying winding play an important role to determine the dynamics. It has been also proven that the distance between the magnetic or electrical souce contributes to the nonlinear force term as well as the current flowing the electromagnet. The other parameters such as resistive load, electromagnet excitation frequency and strength (i.e. current) dominate the dynamics and affect the harvested power in the system. In parallel with the other systems in literature, the natural frequency of the harvester causes maximum power generation. In fact, the nonlinearities in the velocity data for such periodic magnetic excited system subject to decrease the power generation obviously, whereas there exists no remarkable effect of the vibration amplitude on the output power. Considering the methodology of dynamics, many applications of the pendulum-like harvester systems should be realized and both theoretical and experimental explorations should be carried out together in order to draw a complete picture of the applications. The chapter ends with the recent proposed MPPT techniques in order to optimize the harvested power from the piezoelectric systems.

Acknowledgements The supports from Gazi University Research Development Unit under Grant Nos. BAP 07/2010-01, BAP 07/2012-12, Turkey Ministry for EU Affairs—National Agency under Grant No. 2015-1-TR01-KA203-021342 and The Scientific and Technological Research Council of Turkey (TUBITAK) under grant EEEAG-114E017 are acknowledged.

References

1. Tufekcioglu E, Dogan A (2014) A flextensional piezo-composite structure for energy harvesting applications. Sens Actuators A Phys 216:355–363
2. Saha CR, O'Donnell T, Wang N, McCloskey P (2008) Electromagnetic generator for harvesting energy from human motion. Sens Actuators A Phys 147:248–253

3. Ferrari M, Ferrari V, Guizzetti M, Andò B, Baglio S, Trigona C (2010) Improved energy harvesting from wideband vibrations by nonlinear piezoelectric converters. Sens Actuators A Phys 162:425–431
4. Erturk A, Inman DJ (2008) Issues in mathematical modeling of piezoelectric energy harvesters. Smart Mater Struct 17:065016 (14 pp)
5. Lin JH, Wu XM, Ren TL, Liu LT (2007) Modeling and simulation of piezoelectric MEMS energy harvesting device. Integr Ferroelectr 95:128–141
6. Wang L, Yuan FG (2008) Vibration energy harvesting by magnetostrictive material. Smart Mater Struct 17:045009 (14 pp)
7. Poulin G, Sarraute E, Costa F (2004) Generation of electrical energy for portable devices: comparative study of an electromagnetic and a piezoelectric system. Sens Actuators A Phys 116:461–471
8. Rocha JG, Gonçalves LM, Rocha PF, Silva MP, Lanceros-Méndez S (2010) Energy harvesting from piezoelectric materials fully integrated in footwear. IEEE Trans Ind Electron 57:813–819
9. Al-Ashtari W, Hunstig M, Hemsel T, Sextro W (2013) Enhanced energy harvesting using multiple piezoelectric elements: theory and experiments. Sens Actuators A Phys 200:138–146
10. Muralt P, Marzencki M, Belgacema B, Calamea F, Basrourb S (2009) Vibration energy harvesting with PZT micro device. In: Proceedings of the eurosensors XXIII conference, pp 1191–1194
11. Roundy S, Wright PK, Rabaey JM (2004) Energy scavenging for wireless sensor networks. Springer, New York, pp 49–50
12. Caliò R, Rongala UB, Camboni D, Milazzo M, Stefanini C, Petris G, Oddo CM (2014) Piezoelectric energy harvesting solutions. Sensors 14:4755–4790
13. Ward JK, Behrens S (2008) Adaptive learning algorithms for vibration energy harvesting. Smart Mater Struct 17:035025 (9 pp)
14. Priya S (2007) Advances in energy harvesting using low profile piezoelectric transducers. J Electroceram 19:165–182
15. Cho JH, Richards RF, Bahr DF, Richards CD (2006) Efficiency of energy conversion by piezoelectrics. Appl Phys Lett 89:104107 (3 pp)
16. Cottone F, Vocca H, Gammaitoni L (2009) Nonlinear energy harvesting. Phys Rev Lett 102:080601 (4pp)
17. Uzun Y, Kurt E (2013) Power-vibration relation for a piezoelectric harvester under magnetic excitation. In: 13th international conference on electric power system, high voltages, electric mach, Chania, Crete Island, Greece, pp 59–64
18. Uzun Y, Kurt E, Kurt HH (2015) Explorations of displacement and velocity nonlinearities and their effects to power of a magnetically-excited piezoelectric pendulum. Sens Actuators A Phys 224:119–130
19. Kurt E (2006) Nonlinear responses of a magnetoelastic beam in a step-pulsed magnetic field. Nonlinear Dynam 45:171–182
20. Tseng WY, Dugundji J (1970) Nonlinear vibrations of a beam under harmonic excitation. J Appl Mech 37:292–297
21. Tseng WY, Dugundji J (1971) Nonlinear vibrations of a buckled beam under harmonicexcitation. J Appl Mech 38:467–476
22. Poddar B, Moon FC, Mukherjee S (1988) Chaotic motion of an elastic–plastic beam. J Appl Mech 55:185–189
23. Emam SA, Nayfeh AH (2004) Nonlinear responses of buckled beams tosubharmonic-resonance excitations. Nonlinear Dyn 35:105–122
24. Saymonds PS, Yu TX (1985) Counterintuitive behavior in a problem of elastic–plasticbeam dynamics. J Appl Mech 52:517–522
25. Uzun Y, Demirbas S, Kurt E (2014) Implementation of a new contactless piezoelectric wind energy harvester to a wireless weather station. Elektron Elektrotech 20:35–39

26. Uzun Y, Kurt E (2012) Implementation and modeling of a piezoelastic pendulum under a harmonic magnetic excitation. In: 11th international conference on applications of electrical engineering, Athens, Greece, pp 1–6
27. Uzun Y, Kurt E (2013) The effect of periodic magnetic force on a piezoelectric energy harvester. Sens Actuators A Phys 192:58–68
28. Bizon N, Oproescu M (2007) Power converters for energy generation systems (Convertoare de Putere utilizate in Sistemele de Generare a Energiei). Publishing House of the University of Piteşti, Piteşti
29. Bouzelata Y, Kurt E, Altın N, Chenni R (2015) Design and simulation of a solar supplied multifunctional active power filter and a comparative study on the current-detection algorithms. Renew Sust Energ Rev 43:1114–1126
30. Kurt E, Ciylan B, Taskan OO, Kurt HH (2014) Bifurcation analysis of a resistor-double inductor and double diode circuit and a comparison with a resistor-inductor-diode circuit in phase space and parametrical responses. Sci Iran 21:935–944
31. Linsay PS (1981) Period doubling and chaotic behaviour in a driven anharmonic oscillator. Phys Rev Lett 47:1349–1352
32. Kurt E, Kasap R, Acar S (2003) Effects of periodic magnetic field to the dynamics of vibrating beam. J Math Comput Appl 9:275–284
33. Kurt E, Böyükata M, Güvenç ZB (2006) Lyapunov exponent as an indicator of phase transition in melting Pd13 clusters. Phys Scripta 74:353–361
34. Kurt E, Uzun Y (2010) Design and bifurcation analysis of a piezoelectric energy harvester under a changeable magnetic field. In: 2nd international conference on nuclear and renewable energy resources, Ankara, Turkey, pp 877–884
35. Moser RD, Kim J, Mansour NN (1999) Direct numerical simulation of turbulentchannel flow up to Re = 590. Phys Fluids 11:943–945
36. Morris DJ, Youngsman JM, Anderson MJ, Bahr DF (2008) A resonant frequency tunable extensional mode piezoelectric vibration harvesting mechanism. Smart Mater Struct 17:065021 (9 pp)
37. Ramond A, Ardila Rodríguez GA, Durou H, Jammes B, Rossi CA (2009) SIDO buck converter with ultra low power MPPT scheme for optimized vibrational energy harvesting and management. In: PowerMEMS, Washington DC, USA, pp 415–418
38. Kong N, Cochran T, Ha DS, Lin HC, Inman DJ (2010) A self-powered power management circuit for energy harvested by a piezoelectric cantilever. In: 25th applied power electronics conference and exposition (APEC), CA, USA, pp 2154–2160
39. Elliott ADT, Mitcheson PD (2014) Piezoelectric energy harvester interface with real-time MPPT. J Phys Conf Ser 557:012125(5 pp)
40. Yi J, Su F, Lam YH, Ki WH, Tsui CY (2008) An energy-adaptive MPPT power management unit for micro-power vibration energy harvesting. In: IEEE international symposium on circuits and systems, Seattle, WA, USA, pp 2570–2573
41. Simjee F, Chou PH (2006) Everlast: long-life, supercapacitor-operated wireless sensor node. In: Proceedings of the ISLPED, pp 197–202
42. Do XD, Han SK, Lee SG (2014) Optimization of piezoelectric energy harvesting systems by using a MPPT method. In: IEEE 5th international conference on communications and electronics, Danang, Vietnam, pp 309–312
43. Miller LM, Mitcheson PD, Halvorsen E, Wright PK (2012) Coulomb-damped resonant generators using piezoelectric transduction. Appl Phys Lett 100:233901(4 pp)
44. Booth AD (1951) A signed binary multiplication technique. Q J Mech Appl Math 4:236–240